ChemPhysChem

Research Article
doi.org/10.1002/cphc.202300439

Chemistry Europe
European Chemical Societies Publishing

www.chemphyschem.org

VIP *Very Important Paper*

The Prenucleation Equilibrium of the Parathyroid Hormone Determines the Critical Aggregation Concentration and Amyloid Fibril Nucleation

Bruno Voigt,[a] Twinkle Bhatia,[b] Julia Hesselbarth,[c, d] Monika Baumann,[a] Carla Schmidt,[c, d] Maria Ott,[b] and Jochen Balbach*[a]

Nucleation and growth of amyloid fibrils were found to only occur in supersaturated solutions above a critical concentration (c_{crit}). The biophysical meaning of c_{crit} remained mostly obscure, since typical low values of c_{crit} in the sub-μM range hamper investigations of potential oligomeric states and their structure. Here, we investigate the parathyroid hormone PTH_{84} as an example of a functional amyloid fibril forming peptide with a comparably high c_{crit} of 67 ± 21 μM. We describe a complex concentration dependent prenucleation ensemble of oligomers of different sizes and secondary structure compositions and highlight the occurrence of a trimer and tetramer at c_{crit} as possible precursors for primary fibril nucleation. Furthermore, the soluble state found in equilibrium with fibrils adopts to the prenucleation state present at c_{crit}. Our study sheds light onto early events of amyloid formation directly related to the critical concentration and underlines oligomer formation as a key feature of fibril nucleation. Our results contribute to a deeper understanding of the determinants of supersaturated peptide solutions. In the current study we present a biophysical approach to investigate c_{crit} of amyloid fibril formation of PTH_{84} in terms of secondary structure, cluster size and residue resolved intermolecular interactions during oligomer formation. Throughout the investigated range of concentrations (1 μM to 500 μM) we found different states of oligomerization with varying ability to contribute to primary fibril nucleation and with a concentration dependent equilibrium. In this context, we identified the previously described c_{crit} of PTH_{84} to mark a minimum concentration for the formation of homo-trimers/tetramers. These investigations allowed us to characterize molecular interactions of various oligomeric states that are further converted into elongation competent fibril nuclei during the lag phase of a functional amyloid forming peptide.

Introduction

The capability of peptides and proteins to self-assemble into amyloid fibrils is typically associated with their role in neurodegenerative diseases (e.g. Alzheimer's and Parkinson's disease),[1–4] injection amyloidosis (Diabetes type II)[5] or systemic amyloidoses (e.g. antibody light chain amyloidosis).[6] Additionally, so-called functional amyloids are involved in skin pigmentation,[7] bacterial biofilm formation,[8] memory[9] or storage of peptide hormones.[10] Amyloid fibrils assemble via a complex nucleation-dependent network of individual microscopic processes.[11–12] The generation of new individual fibrils can occur via primary nucleation from bulk solution or via surface catalyzed secondary nucleation (Figure 1A).[13–16] Elongation of existing fibrils via addition of new units increases the fibrillar mass.

Nucleation-dependent polymerization is a fundamental principle to describe the process of amyloid generation.[17] In this concept, no assembly is observed below a certain minimum concentration, which is defined as the critical concentration (c_{crit}).[17–19] The concentration of free peptide in the thermodynamic equilibrium with fibrils is also reflected by c_{crit}.[20] This can be experimentally determined e.g. by sedimentation of the fibrils with a subsequent quantification of the soluble protein fraction or by diluting fibrils which, as a consequence, release monomers until c_{crit} is reached.[21–23] Protein solutions exceeding c_{crit} are supersaturated, metastable and kinetically soluble.[24–25] With time, the nucleated conversion into amyloid fibrils is a key feature of such metastable states.[19] A crucial step for primary nucleation of an amyloid structure is the formation of

[a] B. Voigt, Dr. M. Baumann, Prof. Dr. J. Balbach
Martin Luther University Halle-Wittenberg
Institute of Physics
Betty-Heimann-Straße 7, 06120 Halle (Germany)
E-mail: jochen.balbach@physik.uni-halle.de

[b] T. Bhatia, Dr. M. Ott
Martin Luther University Halle-Wittenberg
Institute of Biochemistry and Biotechnology
Kurt-Mothes-Straße 3, 06120 Halle (Germany)

[c] J. Hesselbarth, Prof. Dr. C. Schmidt
present address: Johannes Gutenberg University Mainz
Institute of Chemistry – Biochemistry, Biocenter II
Hanns-Dieter-Hüsch-Weg 17, 55128 Mainz (Germany)

[d] J. Hesselbarth, Prof. Dr. C. Schmidt
Martin Luther University Halle-Wittenberg
Interdisciplinary Research Center HALOmem, Institute of Biochemistry and Biotechnology
Kurt-Mothes-Straße 3a, 06120 Halle (Germany)

Supporting information for this article is available on the WWW under https://doi.org/10.1002/cphc.202300439

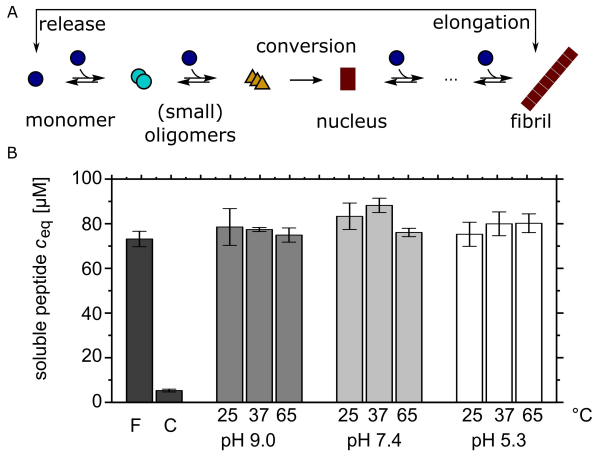

Figure 1. A – Simplified model of amyloid fibril growth involving oligomeric species for primary nucleation. **B** – Monomer release from pre-formed PTH_{84} fibrils at 24 h in 50 mM sodium borate (pH 9.0), 50 mM sodium phosphate containing 150 mM sodium chloride (pH 7.4) or 10 mM Bis-Tris (pH 5.3). F: c_{eq} of the initial fibril sample, C: soluble peptide directly after resuspension of washed fibrils.

prefibrillar oligomers convertible into nuclei which finally grow to fibrils by monomer addition.[26–27]

Oligomers in the context of amyloid self-assembly display a varying relevance to fibril formation.[26] On-pathway oligomers are able to directly contribute to amyloid nucleation or growth, while off-pathway oligomers need to dissociate first. For example, the Huntingtin exon 1 protein htt^{ex1} and other constructs of this protein were found to be predominantly monomeric with transient populations of an off-pathway dimer as well as with an on-pathway dimer and tetramer preceding nucleation.[28–29] In addition to this function as precursors for nucleation, oligomers have been found to be the species involved in fibril elongation e.g. for the truncation variant ΔN6 of human β_2-microglobulin.[30–32] So-called globular oligomers are also described to result in alternative pathways as precursors for the formation of curvilinear fibrils above a critical oligomer concentration (coc) for an artificial dimeric Amyloid β peptide (dimAβ) and lysozyme, in contrast to rigid fibrils originating from nucleated polymerization below the coc.[33–34]

Although there are many studies investigating oligomer formation during amyloid growth,[26,35] only a few reports analyzed possible transitions of the secondary structure and oligomer sizes of a peptide at c_{crit} to investigate the influence of supersaturation on biophysical properties of peptides.[36] In most cases c_{crit} is below experimental limits, e.g. in the pM to low µM range for $A\beta_{40}$.[24]

In this work we present an in vitro approach to biophysically characterize c_{crit} for amyloid fibril formation. For this purpose, we use the parathyroid hormone in its mature state bearing 84 residues (PTH_{84}).[37] The hormone which acts in blood calcium and phosphate homeostasis is hypothesized to be stored in functional amyloid fibrils in secretory granules prior to its release into the blood stream.[21,38] The N-terminal part of PTH_{84} displays an α-helical propensity while the C-terminal part remains disordered.[39–42] PTH_{84} offers a reversible fibrillation system with c_{crit} in a µM concentration range which is easily accessible by a variety of biophysical techniques.[21–23] The secondary structure and oligomerization propensity of PTH_{84} below, near and above c_{crit} are investigated at conditions at which the peptide self-assembles into fibrils to characterize potential transitions as a consequence of supersaturation. We show that the prenucleation state of PTH_{84} comprises equilibria involving oligomers of different molecular weights dependent on the total concentration c_0. Here, c_{crit} marks a transition from a monomer-dimer equilibrium ($c_0 < c_{crit}$) towards an equilibrium involving a trimeric and tetrameric state ($c_0 > c_{crit}$) which we suspect to contribute to primary nucleation. We additionally demonstrate that the monomer-dimer equilibrium persists in the presence of fibrils, thus revealing an important insight into the origin and role of c_{crit} and the early mechanism of amyloid formation.

Results

The Critical PTH_{84} Concentration is not Affected by Buffer Conditions

The parathyroid hormone PTH_{84} is able to self-assemble into amyloid-like fibrils with a reported c_{crit} of 67 ± 21 µM.[21] To test whether c_{crit} depends on external factors, we performed monomer release assays from pre-formed fibrils (Figure 1B). For reversible assemblies, monomers are released from fibrils upon dilution until c_{crit} has been approached. Interestingly, independent from pH (pH 9.0, pH 7.4, pH 5.3), temperature (25 °C to 65 °C) or buffer systems (phosphate, Bis-Tris, borate), the individually determined concentration of soluble peptide (c_{eq}) always increased to 79 ± 4 µM after 24 h of incubation. This relates to a robust c_{crit} of PTH_{84} that is unaffected by ample changes of the environment.

Furthermore, c_{crit} can be used as a measure of the Gibbs free energy for the overall fibrillation process with $\Delta G^0 = -RT \cdot \ln(1\ Mc_{crit}^{-1}) = -23.8\ kJ\,mol^{-1}$ at 25 °C.[19,43] The high value of c_{crit} reflects the low thermodynamic stability of PTH_{84} fibrils. For comparison, ΔG^0 of $A\beta_{40}$ and $h\beta_2m$ is reported to be $-36.0\ kJ\,mol^{-1}$ and $-33.0\ kJ\,mol^{-1}$, corresponding to c_{crit} of 0.9 µM and 2.7 µM, respectively.[18,44]

Biophysical PTH_{84} Properties Depend on the Peptide Concentration

To characterize c_{crit} on the molecular level we examined the biophysical properties of PTH_{84} in a broad concentration range below and above c_{crit}. In agreement with experimentally determined structures,[40,42] AlphaFold 2.0 predicted an α-helix for residues E4-L37, an intrinsically disordered C-terminal part, and an additional α-helix for residues K72-A81 (Figure 2A).[39,41] The latter α-helix was not experimentally observed.[42] For a detailed analysis of possible c_0 effects on the structure we used the intrinsic W23 fluorescence ratio F_{350}/F_{320} as an indicator for spectral changes. Within the c_0 range probed, four different

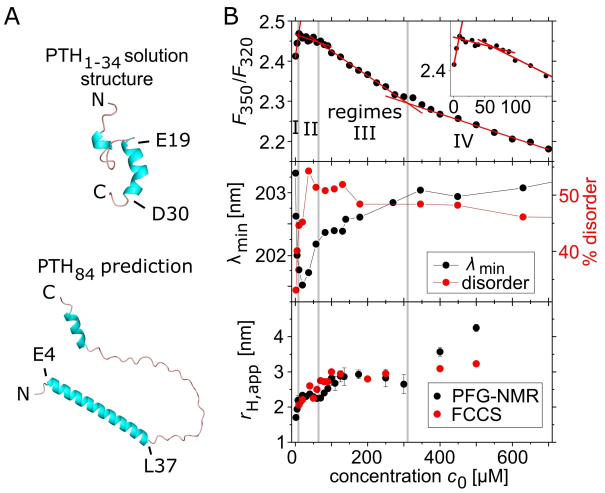

Figure 2. Structural and hydrodynamic properties of PTH_{84} at various concentrations. **A** – cartoon sketch of $PTH_{1\text{-}34}$ (pdb-code 1zwa) (top) and AlphaFold 2.0 predicted structure of PTH_{84} (bottom),[39–41] **B** – intrinsic tryptophan fluorescence shown as the ratio F_{350}/F_{320} (upper panel). The red lines are linear fits to the respective data within the four regimes. The inset enlarges the range of low c_0. Analysis of far-UV CD spectra (middle panel), shown are the wavelengths of the CD minimum $\lambda_{min,1}$ around 202 nm (black) and the estimated content of disordered regions (red, deconvolution performed with BESTSEL). The apparent hydrodynamic radius $r_{H,app}$ (lower panel) was determined by PFG-NMR (black) and FCCS (red).

concentration regimes were identified (Figure 2B, upper panel): (a) $c_0 < 10$ μM (regime I), (b) 10 μM $< c_0 <$ 70 μM (regime II), (c) $70 < c_0 < 310$ μM (regime III) and $c_0 > 310$ μM (regime IV). Note that the transition between regimes II and III occurred at c_{crit}. The observed decrease of F_{350}/F_{320} for regimes II, III and IV indicates a shift of the maximum fluorescence $\lambda_{em,max}$ towards lower emission wavelengths (Figure S1A). This behavior refers to a decreased solvent accessibility of the W23 environment resulting either from intra- (conformational reorientation) or intermolecular interactions (oligomer formation). For regime I we found a positive slope indicating the opposing effect of a decreasing hydrophobicity of the W23 environment with c_0.

The general appearance of the circular dichroism (CD) spectra displaying a dominant minimum at $\lambda_{min,1} \approx 202$ nm and a minor minimum at $\lambda_{min,2} \approx 220$ nm is indicative of an intrinsically disordered peptide with additional contributions from an α-helix (Figure S1B).[21–22,42] In contrast, a CD spectrum calculated from the predicted structure (Figure S1B) shows the typical minima of α-helices at $\lambda_1 = 208$ nm and $\lambda_2 = 220$ nm, indicating an overestimation of the α-helix content by AlphaFold 2.0.[45] To monitor c_0 dependent effects, we used the evolution of the CD minimum wavelength $\lambda_{min,1}$ as an indicator for disorder ($\lambda =$ 195 nm) and α-helical structure formation ($\lambda = 208$ nm) (Figure 2B, middle panel). For regime I we found a shift of $\lambda_{min,1}$ from 203.3 nm towards 201.7 nm with increasing c_0. This small but notable systematic shift indicates an increase of disorder, which is supported by a BESTSEL analysis (red in the same Figure).[46] Simultaneously, the apparent hydrodynamic radius $r_{H,app}$ increased from 1.7 ± 0.1 nm to 2.1 ± 0.1 nm as observed by pulsed field gradient (PFG)-NMR and fluorescence cross-correlation spectroscopy (FCCS) (Figure 2B, lower panel, and Figure S2). Interestingly, $r_{H,app}$ remained constant within regime II, while $\lambda_{min,1}$ increased again towards 202.3 nm. Obviously, within regime II the structure of PTH_{84} is affected by c_0 without an observable change in size. The major red shift of $\lambda_{min,1}$ continued for regime III. Meanwhile, $r_{H,app}$ increased until $c_0 =$ 125 μM towards 2.9 nm, but remained constant for higher c_0. In regime IV we observed a proceeding minor red shift of $\lambda_{min,1}$ and a strong increase of $r_{H,app}$ to 4.2 nm or 3.5 nm as determined by PFG-NMR and FCCS, respectively. The BESTSEL analysis of the CD spectra for regimes II–IV revealed that the observed shift of $\lambda_{min,1}$ indicates a slight decrease of disordered structure.

In summary, PTH_{84} exhibits a compact state with a higher degree of secondary structure at low c_0 which becomes more extended with increasing c_0, supported by an increased solvent accessibility of W23. The positive trend of Θ_{MRW} at $\lambda_{min,}1$ (Figure S1B) suggests that PTH_{84} evolves from an intrinsically disordered peptide (IDP) with α-helical propensity at low c_0 (regime I) towards an IDP with decreased helix propensity at high c_0 (regime IV). The trend of a strongly increasing ensemble $r_{H,app}$ indicates a monomer-oligomer equilibrium with different secondary structural compositions and transient species in fast dynamic exchange.[30]

PTH_{84} Monomers are in Equilibrium with Oligomers of Peptide Concentration Dependent Sizes

Next, we asked if the c_0 dependent increase of the ensemble $r_{H,app}$ occurs due to conformational changes resulting in an extended structure or due to oligomer formation. In order to reveal possible size distributions, we used small angle X-ray scattering (SAXS) with a subsequent ensemble optimization analysis (EOM, Figure 3A and Figure S3) to investigate the distributions of the radii of gyration (r_G) at 50 μM (regime II) and 500 μM (regime IV). The corresponding end-to-end distances (r_{ee}) were obtained by dual-color single-molecule fluorescence resonance energy transfer (smFRET, Figure 3B and Figure S4). For regime II, SAXS revealed two states with distinct, narrow distributions of r_G (2.1 ± 0.2 nm and 2.8 ± 0.2 nm) while only one r_{ee} distance (5.7 nm) was detected by smFRET. We suspect that both r_G states either display a monomeric and an oligomeric state while r_{ee} of the involved individual peptide chains remain unchanged or two conformational states that interconvert on a timescale < 200 μs. Exceeding c_{crit}, the values of both r_G maxima increase (2.4 ± 0.2 nm and 3.0 ± 0.3 nm), indicating different dynamic equilibria for the probed c_0 regimes as well as a possible under-representation of monomers in the scattering intensity curves. Interestingly, smFRET experiments for regime IV also revealed two states. The r_{ee} of the dominant state increased only marginally with c_0 from 5.7 to 5.9 nm, while an additional, extended state with $r_{ee} = 7.5$ nm was found with 22% amplitude which was not detected by the EOM analysis.

Independently, we applied native mass spectrometry (MS) allowing the direct observation of oligomers. For regime I ($c_0 =$ 10 μM), we obtained a charge state distribution corresponding to a molecular mass of 9424 g mol^{-1} (Figure 3C, upper panel, $M_{W,PTH84} = 9424.7$ g mol^{-1}),[47] revealing PTH_{84} to be monomeric at

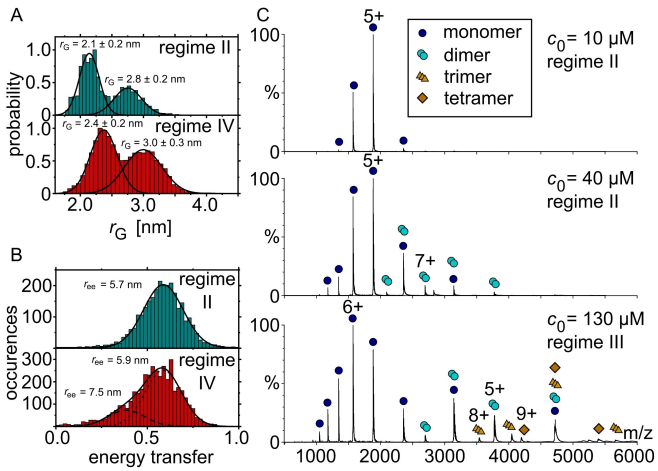

Figure 3. Analysis of PTH_{84} oligomerization. **A** – EOM analysis of the X-ray scattering profiles for 50 µM (upper panel) and 500 µM (lower panel). **B** – smFRET determined energy transfer histograms for 50 µM (upper panel) and 500 µM (lower panel). **C** – native mass spectrometry of PTH_{84} at 10 µM (upper panel), 40 µM (middle panel) and 130 µM (lower panel). The observed charge state distributions correspond to monomers (blue circles), dimers (cyan circles), trimers (orange triangles) and tetramers (orange squares). The respective molecular masses are given in the main text. After incubation, the buffer was exchanged to 200 mM $(NH_4)CH_3COO$ directly prior to the measurement.

low c_0. However, at 40 µM (regime II) a second series of charge states was observed which can be assigned to an 18848 g mol^{-1} particle, equal to the molecular weight of a PTH_{84} dimer (Figure 3C, middle panel). This was successfully confirmed by selecting the 7+ charge state of the dimer as a precursor for dissociation experiments (Figure S5). Thus, the two r_G states in SAXS-EOM in regime II refer to a PTH_{84} monomer and a dimer. Further increasing c_0 (regime III) resulted in additional charge state series corresponding to a PTH_{84} trimer (28280 g mol^{-1}) and tetramer (37754 g mol^{-1}, Figure 3C, lower panel).

Together, SAXS, smFRET and native MS confirmed that PTH_{84} is solely monomeric only at regime I and exhibits a monomer-oligomer equilibrium at other regimes, with c_0 dependent cluster sizes. Most notably, above c_{crit} (regime III) additionally to dimeric PTH_{84} a trimeric and a tetrameric species were observed by native MS. For regime IV, we suppose the formation of an oligomer of high molecular weight, supported by a strong increase of $r_{H,app}$ in this regime as well as a second extended r_{ee} state.

The N-terminus of PTH_{84} Facilitates Oligomer Formation

Two-dimensional NMR spectroscopy allows to derive residue specific information about which segments of PTH_{84} are involved in inter- and intramolecular interactions. The low dispersion within the proton dimension of cross-peaks in our c_0 dependent backbone ^{1}H-^{15}N-fHSQC spectra (Figure 4A) agrees with a predominantly disordered peptide with transient α-helices.[21,42,48] Notably, we observed a c_0 dependent perturbation of the chemical shift (CSP) or the detected signal intensity for many cross-peaks. Gradually shifting cross-peaks typically indicate the co-existence of two or more distinct NMR detectable states in the fast chemical exchange regime on the sub-millisecond time scale.

For regime I we detected unspecific CSP for all residues (Figure 4B upper and middle panel, and Figure S6), while a significant decrease of intensity was only observed for residues L15-K27 which bear a basic RKK patch. Note that W23, sensing an increasing hydrophilicity of the environment (Figure 2B, upper panel), is in the same region. Additionally, the basic residues 50R-54K, which contain a second RKK patch, display a small but systematic intensity increase. In regimes II–IV, cross-peak intensity as well as CSP were most affected within the N-terminal region (residues S1-A42) of PTH_{84} while little or no effect was detected for the disordered C-terminal region (R44-Q84). Interestingly, within regimes III and IV the CSP for V35-G38 increased compared to the other residues indicating a pronounced participation of this sequence in PTH_{84} interactions.

Except for regime I, we observed additional minor cross-peaks in close proximity to the signals corresponding to V35, G38, and A39 (insets in Figure 4A). The occurrence of two distinct peaks indicated an additional equilibrium of states in the slow exchange limit. Since these minor cross-peaks were observed in a regime for which we found dimer formation, we attribute them to a dimeric state of PTH_{84}. All three residues are situated in a highly hydrophobic region of PTH_{84} (^{34}FVALGAP^{41}LA), indicating that hydrophobic interactions are most probably involved in dimer formation. Additionally, the CSP of the corresponding major cross-peaks strongly modulated with c_0, especially in regimes III and IV (Figure S6). This indicates that this peptide region senses, at least, two equilibria: one in the fast, the other in the slow exchange regime of the NMR chemical shift time scale. We suppose that hydrophobic interactions are also relevant for trimer/tetramer and high-order oligomer formation observed in regimes III and IV.

In order to analyze whether the intensity changes originate from differences of local dynamics or oligomer formation we determined the longitudinal (R_1) and transversal relaxation rates (R_2) at the different c_0 regimes. The R_2/R_1 ratio is sensitive to changes of the local peptide rotational correlation time τ_c on a nanosecond time scale and chemical exchange on a millisecond time scale. This is a valuable NMR parameter to reveal transient local structure formation especially of IDPs.[49–50] In general, PTH_{84} displayed a higher R_2/R_1 ratio for residues L7-G38 compared to other residues (Figure 4B, lower panel). This indicated a propensity for the formation of secondary structure in this region, in good agreement with reported structures.[39–42] With increasing c_0, R_2/R_1 strongly increased for regimes III and IV. We attribute this up to six-fold increase mainly to the formation of oligomers with a larger τ_c and to an additional exchange contribution (R_{ex}) to the transversal R_2 relaxation ($R_{2,obs} = R_2^0 + R_{ex}$). The latter arises from a fast interconversion of states on a millisecond time scale.[51] Interestingly, no difference of R_2/R_1 was observed between $c_0 = 20$ µM and 100 µM, although a strong decrease of the relative peak intensities was found. Again, residues L41-Q84 did not show c_0 effects on relaxation, indicating that this segment remains flexible in oligomeric PTH_{84} states.

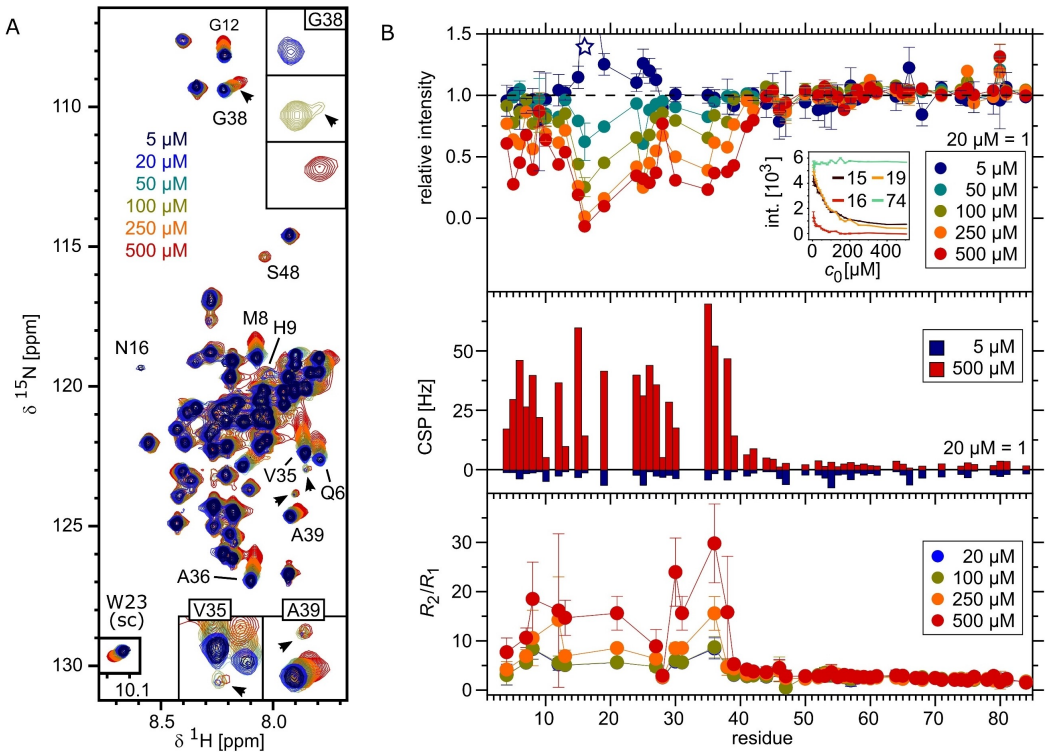

Figure 4. Concentration dependent NMR characterization of PTH_{84}. **A** – ^{1}H-^{15}N-HSQC of ^{15}N enriched PTH_{84} at 5 µM, 20 µM, 50 µM, 100 µM, 250 µM and 500 µM. The assignments of selected cross-peaks with strong CSP are given. Additional cross-peaks for V35, G38 and A39 are indicated by black arrows (arrow for G38 points at additional cross-peak at 50 µM (blue-green)). The insets enlarge spectral regions near V35, G38 and A39 focusing on the additional minor cross-peaks. **B** – Relative intensities of cross-peaks at 5 µM, 100 µM, 250 µM and 500 µM (upper panel), CSP for 5 µM (displayed as negative values) and 500 µM compared to 20 µM (middle panel). The respective values for 20 µM are set to unity to compare changes for the monomer-related effects (regime I, $c_0 < 20$ µM) and additional effects from the oligomerization equilibrium (regimes II–IV, $c_0 > 20$ µM). Relaxation properties at 20 µM, 100 µM, 250 µM and 500 µM are displayed in the lower panel. R_2/R_1 ratios are almost identical for $c_0 = 20$ µM and 100 µM. The inset in the upper panel displays absolute intensities (Equation 9) for L15, N16, E19 and D74. The relative intensity of N16 for 5 µM compared to 20 µM is 2.4 ± 0.8, a high value which might be due to low absolute intensity of the N16 cross-peak (red in the inset). Adjacent residues L15 (dark red) and N19 (orange) show a similar intensity decrease with c_0 and follow the same trend in the relative intensity. We displayed the relative intensity data point of N16 with a star indicating a high value in the trend of nearby residues but with high uncertainty.

The Soluble Peptide in Equilibrium with Fibrils Adopts the Same State as Without Fibrils

Last, we asked if the soluble PTH_{84} fraction in equilibrium with its fibrils is monomeric or adopts to the prenucleation state. For this purpose, we recorded ^{1}H-^{15}N-fHSQC spectra of samples with ^{15}N labeled PTH_{84} (c_0: 100 µM, 300 µM and 500 µM) before and after addition of 5% unlabeled PTH_{84} fibrils (given in monomer equivalents) to induce seeded growth (Figure 5A). After 7 days of incubation c_{eq} was found to be 51.3 µM ($c_0 = 100$ µM), 69.2 µM ($c_0 = 300$ µM) and 52.2 µM ($c_0 = 500$ µM), in good agreement with c_{crit} (Figure 1B). We compared the chemical shift differences of the resulting cross peaks with the respective cross-peak positions obtained from a set of reference spectra without fibrils. The root mean square deviation (RMSD) was used to determine the pair of spectra with minimal CSP (Equation 10). Without fibrils, the RMSD values displayed minima at 100 µM, 300 µM and 500 µM, respectively, indicating that these spectra are most similar to the reference spectra acquired at the same c_0 as the samples (Figure 5A, closed circles, and Figure S7). In equilibrium with fibrils, we found minimum RMSD values at appr. 40 µM for all c_0. Thus, the resulting spectra in the presence of fibrils are most similar to the spectrum obtained from 40 µM PTH_{84} without fibrils (Figure 5A, open circles), a concentration which agrees well with the obtained c_{eq}.

In order to learn more about the adaption of the free peptide to monomer consumption by fibril elongation, we investigated the evolution of the 2D fHSQC cross-peak pattern during seeded fibril growth at $c_0 = 250$ µM (regime III) and 500 µM (regime IV) (Figure 5B). For all time points and for both c_0, the RMSD minima closely corresponded to the concentration of the soluble peptide as determined by 1D ^{1}H NMR. We propose from these RMSD analyses and time-resolved NMR data that peptide consumption by fibril elongation does not lead to monomer depletion with a remaining oligomeric fraction. Instead, the dynamic equilibrium is readily re-established according to the available concentration of soluble peptide.

Finally, we analyzed the local backbone dynamics of the soluble state in equilibrium with fibrils (Figure S8). For residues L10-D30 we found a small and for residues A70-Q84 a very small but systematic increase of R_2/R_1 compared to the sample without fibrils. This increase indicates weak interactions of these

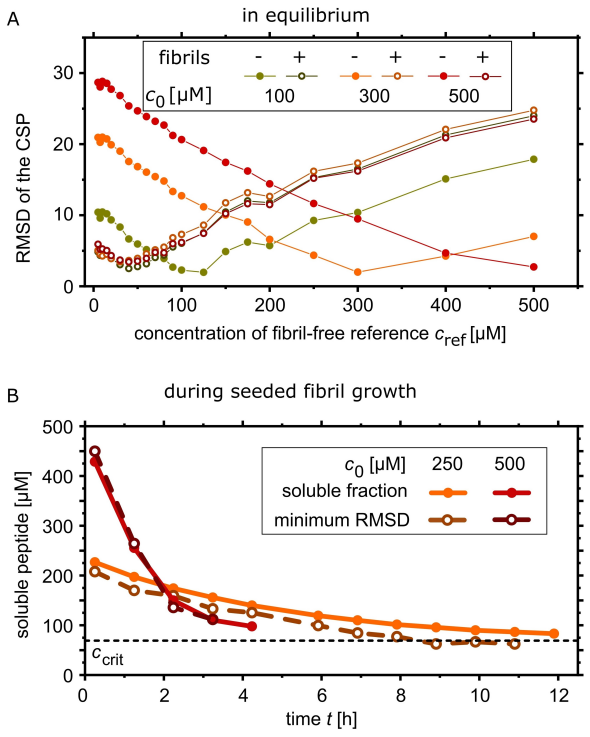

Figure 5. NMR characterization of PTH_{84} in the presence of fibrils. **A** – RMSD of backbone chemical shifts in ^{1}H-^{15}N-fHSQC spectra of samples with $c_0 = 100$ µM (dark yellow), 300 µM (orange) and 500 µM (red) without (closed circles) and in equilibrium with fibrils (open circles) compared to reference spectra acquired in the absence of fibrils. **B** – 1D ^{1}H and 2D ^{1}H-^{15}N-fHSQC detected seeded fibril growth at initial peptide concentrations of 250 µM (orange) and 500 µM (red). 1D ^{1}H intensity analysis to extract the concentration of free PTH_{84} (closed circles) and the corresponding minimum RMSD of the CSP, compared to the prenucleation equilibrium (open circles) for each time point. The y-axis displays the concentration of the soluble peptide and the reference spectrum showing the lowest respective RMSD. For clarity, RMSD values are displayed in a darker color than the free peptide concentration. The black dashed line indicates the critical concentration c_{crit}.

sections of soluble PTH_{84} with the fibrils at the fibril surface or growth-competent ends due to association and dissociation in equilibrium. Thus, slower local tumbling or chemical exchange increases transversal R_2 relaxation. This supports the hypothesis that fibrils do not induce additional conformational or oligomeric states.

Discussion

In the present work we investigated c_0 dependent secondary structure and the monomer-oligomer equilibrium of PTH_{84} to biophysically characterize c_{crit} of amyloid formation. The identification of four c_0 regimes, characterized by distinct biophysical signatures with transition concentrations at ~10 µM, ~70 µM and ~310 µM, was a remarkable finding of our study.

Many experimental reports of C-terminally truncated variants of PTH_{84}, as well as structure prediction, consistently assign an α-helix for residues E4-L37 for the peptide monomer. A recent NMR study confirmed the helix propensity for PTH_{84} at pH 5.3.[42] At pH 7.4, we found PTH_{84} to be solely monomeric only at very low c_0 (regime I). An increase of c_0 within this regime resulted in an increase of structural disorder coupled to an expansion of the chain. Interestingly, only the backbone NMR intensities of residues L15-K27 were affected.

For regime II, PTH_{84} is in equilibrium with its homo-dimeric form, as indicated by native MS and SAXS-EOM leading to NMR detectable changes in the N-terminal region (residues E4-G38). The fraction of dimeric species was not sufficient to significantly increase the ensemble r_H. Nevertheless, the overall content of secondary structure was again increased. The transition from regime II to regime III was characterized by the occurrence of an additional homo-trimer/tetramer and coincided with c_{crit} of PTH_{84} fibrillation. In the high c_0 range, an additional state was observed with increased r_H (PFG-NMR and FCCS), higher r_G (SAXS-EOM) and larger r_{ee} (smFRET) compared to the lower c_0 regimes. Within the framework of our previous reported mechanism of PTH_{84} fibril formation,[23] we propose that the trimer or tetramer acts as precursor for primary nucleation at low c_0 (<310 µM, regime III), since these oligomers only appeared above c_{crit}. The previously calculated reaction order for primary nucleation n_1, being related to the physical nucleus size, of $2 \leq n_1 \leq 4$ supports such oligomer sizes.[23] Interestingly, fibrillation was found to proceed with lag-times (t_{lag}) of approximately 175 h ($c_0 = 100$ µM) decreasing with increasing c_0 until fibrillation apparently becomes c_0 independent at 250 µM ($t_{lag} \approx 110$ h). Below c_{crit} (regime II), no fibril formation was observed. The high-order oligomer at regime IV, as previously hypothesized from kinetic experiments and supported by smFRET, FCCS and PFG-NMR in this work, is suspected to be the nucleation precursor at high c_0 (>310 µM). For this c_0 regime we found a switch of the reaction order of primary nucleation towards $n_1 = 18.5$, enabling a competition with secondary nucleation.[23] This led to a considerable reduction of the lag-time to about 60 h for $c_0 = 500$ µM and further to ca. 20 h for $c_0 = 600$ µM. Importantly, in the current report we used an incubation time of 18 h to ensure an equilibrium between monomeric and oligomeric species.

Native MS revealed an equilibrium of PTH_{84} monomers with oligomers of low molecular weight while only one corresponding r_{ee} fraction was found. From smFRET we suspect that peptides in monomers and small oligomers display comparable chain dimensions, but adopt a more extended conformation in high order oligomers (regime IV). Such extended conformational states were also found for the tau protein[52] and α-synuclein[53] within liquid-liquid phase separated solutions facilitating intermolecular cluster formation leading to amyloid fibril formation. Indeed, our CD analysis indicated a conformational reorientation with a decreasing α-helical propensity of the N-terminal region in the high c_0 regime.

Two-dimensional NMR spectroscopy allowed us to get to residue resolution and dynamic aspects of PTH_{84} states. We not only found gradual CSP, indicating a fast, dynamic equilibrium between at least 2 states, but also additional cross-peaks for residues V35-A39, indicating a second, slow equilibrium in regimes II to IV. Our c_0 series probing the ensemble relaxation properties R_2/R_1 agree with a strongly decreased rotational correlation time τ_c as a consequence of oligomerization at high

c_0 as well as an exchange contribution R_{ex} due to fast equilibria. Interestingly, R_2/R_1 was almost identical for 20 μM (regime II) and 100 μM (regime III), consistent with the slow-exchange regime at which R_{ex} has only marginal effects on transversal relaxation. Note that $r_{H,app}$ (PFG-NMR) did also not change within regime II but CSPs were still observed. The additional cross-peaks for V35-A39, situated in a hydrophobic sequence, were detectable for regimes II to IV with a low signal intensity and even persisted in equilibrium with fibrils. We suspect that this refers to a dimeric species which is formed via weak hydrophobic interactions and is most probably non-productive for fibrillation. A similar network of sparsely populated productive dimers and tetramers as well as a non-productive dimer has also been described for the Huntington's disease related protein huntingtin (htt).[29,54–55]

In our NMR-experiments, only little to no effects were observed for the disordered C-terminal part of PTH_{84}, while resonance intensity, CSP and relaxation were considerably affected within the N-terminal part. Under the neutral pH conditions used in this study, the major fraction of histidine residues is expected to be in the deprotonated state due to the side chain N–H pK_a value of 6.45.[56–57] Of the 4 histidines of PTH_{84} (H9, H14, H32, H63) only H9 displayed an assignable cross-peak with a low intensity at pH 7.4.[58] In contrast, at pH 5.3 ($pH < pK_{a,His}$) all histidine residues were detectable.[21,42] This fact hints towards a possible participation of histidine in such interactions. The response of both PTH_{84} RKK patches as a consequence of c_0 increase within regime I, in which PTH_{84} is monomeric but expanding, suggests contributions from these motifs. The helical parts are probably stabilized by weak intramolecular cation-π interactions of basic side chains with, e.g., histidine or π-π interactions involving histidine and arginine residues,[59–62] also in the disordered part. The expansion of the chain coupled to the loss of secondary structure possibly occurs due to intermolecular transient interactions which further lead to oligomer formation.

We would like to highlight that soluble PTH_{84} adopts the same monomer-dimer equilibrium after fibril formation as in the prenucleation state of appr. 40 μM (regime II), close to c_{crit}. This was not only observed for the thermodynamic equilibrium, but also during seeded fibril growth, indicating that the described oligomers are not static aggregates. The CSP of free, soluble PTH_{84} readily adopted to the prenucleation situation at corresponding c_0. Fibrils obviously do not affect the soluble state in terms of additional structure or oligomer formation. The small effect on R_2/R_1 ratios in equilibrium with fibrils for G12-V31 and A70-Q84 hint towards weak interactions of soluble peptides with the fibril surface, supporting our previous hypothesis.[23] Monomer-fibril interactions are a common feature of amyloid systems and have been described in detail e.g. for $A\beta_{40}$.[63–64]

To our knowledge, this is the first report of a c_0 dependent rapid oligomerization equilibrium of an aggregation-prone peptide specific for c_{crit}, which persists also in the presence of amyloid fibrils. The long lag-times agree with a very slow conversion step of the oligomers into fibril nuclei.[23] We suppose that the considerably smaller lag-times for e.g. $A\beta_{40}$ indicate a slower oligomerization but a fast conversion rate which is possibly related to the toxicity of $A\beta_{40}$ oligomers.[65–66]

Experimental Section

Material. All chemicals were purchased from Sigma Aldrich or Carl Roth GmbH and used without further purification.

Recombinant Production of PTH_{84} and sample preparation. The recombinant production of PTH_{84} was conducted according to the previously published protocol.[23] For 2D-NMR experiments, cells were grown in minimal salt medium with $^{15}NH_4Cl$ as the only source of nitrogen.[67] For single molecule techniques, double labelled Atto488-maleimide-cysteine-PTH_{84}-propargyl-glycine-Atto594-azid-OH was synthesized by the Core Unit Peptide Technologies of the University of Leipzig as published previously.[22,68] Aliquots of the stock solution were allowed to thaw on ice, centrifuged (16000 g, 10 min, room temperature), diluted to the respective peptide concentration and supplemented with 150 mM NaCl for all analytical methods. The final buffer composition used for all experiments, if not stated otherwise, was 50 mM Na_2HPO_4, 150 mM NaCl, pH 7.4. All experiments have been conducted at 25 °C. For all experiments, the recombinantly produced PTH_{84} was used. Synthetic PTH_{84} double-labelled with fluorescent tags was additionally added for detection in single-molecule fluorescence techniques, as stated below.

Reversibility assay. Fibrils were grown by incubation of 700 μM PTH_{84} in 50 mM Na-Borate, pH 9.0 for 18 h at 65 °C.[21] After sedimentation (1 h, 16200 g), the supernatant was carefully removed, fibrils were resuspended in the same amount of Borate buffer, sedimented again and resuspended in borate buffer (pH 9.0), 50 mM Na_2HPO_4 (pH 7.4) or 10 mM BisTris, 300 mM Na_2SO_4 (pH 5.3) and incubated at 25 °C, 37 °C or 65 °C for 24 h. After sedimentation, the equilibrium monomer concentration within the supernatant was determined by UV/Vis spectroscopy on a J-650 spectrophotometer (Jasco International Co., Ltd., Tokyo, Japan).

CD spectroscopy. For estimating the overall amount of secondary structure, circular dichroism (CD) spectroscopy was used. In order to maintain a valuable signal-to-noise ratio, the detector tension (HT) and absorbance were kept below 600 V or 0.4, respectively. As a consequence, different cuvettes with different path lengths (d) were used: $d = 1$ mm ($c_0 < 20$ μM), $d = 0.1$ mm (20 μM $< c_0 <$ 150 μM) and $d = 0.01$ mm ($c_0 > 150$ μM). For each sample 15 individual scans with a scanning speed of 50 nm/min and a bandwidth of 1 nm were accumulated on a J-815 spectropolarimeter (Jasco International Co., Ltd., Tokyo, Japan). The mean residue ellipticity, Θ_{MRE}, was calculated as

$$\Theta_{MRE} = \frac{\Theta}{10\ c_0\ d\ N_{aa}} \quad (1)$$

with Θ the measured ellipticity, c_0 protein concentration, d the path length and N_{aa} the number of residues within the peptide. A decomposition to extract information on structural content was performed by BESTSEL.[46] Since PTH_{84} is predominantly disordered, our analysis focuses on "other" structures which we interpret as unstructured content. A theoretical CD spectrum has been calculated from the AlphaFold 2.0 predicted three-dimensional structure of PTH_{84} by using the PDBMD2CD server.[69]

Intrinsic tryptophan fluorescence spectroscopy. Intrinsic PTH_{84} W23 fluorescence was recorded ($\lambda_{exc} = 280$ nm, $\lambda_{em} = 290$–550 nm, scanning speed 50 nm/min) on a FP-6500 fluorescence spectrometer (Jasco International Co., Ltd., Tokyo, Japan). For analysis, the

fluorescence ratio F_{350}/F_{320} was used. As a consequence of the high peptide concentrations used, the fluorescence intensity at only one emission frequency is possibly biased due to primary inner filter effects, whereas the ratio monitors concentration dependent changes with respect to the spectral form. In the absence of changes to the spectral shape the trend of this ratio is expected to be linear. Whereas intermolecular quenching effects of W23 possibly contribute to spectral changes, intramolecular effects due to F34 should be negligible.

Native mass spectrometry (native MS). Using a mass spectrometer modified for transmission of high masses,[70] proteins and complexes thereof are transferred intact into the gas phase by preserving non-covalent interactions. Thus, the oligomeric state can directly be observed.[71] The storage buffer of 20 μL PTH_{84} was exchanged to 200 mM ammonium acetate using Micro Bio-Spin 6 gel filtration columns (BioRad). 4 μL of 10–130 μM PTH_{84} were loaded into gold-coated glass capillaries prepared in-house[72] and directly introduced into a Waters Micromass Q-ToF Ultima mass spectrometer modified for transmission of high masses.[70] For data acquisition the following parameters were used: capillary voltage 1.3–1.7 kV, sample cone voltage 80 V, RF lense voltage 80 V, collision voltage 20–50 V. Mass spectra were processed using MassLynx 4.1 software (Waters) and were externally calibrated using 100 mg/ml caesium iodide solution. Mass spectra were assigned using MassLynx 4.1 and Massign software (version 11/14/2014).[73]

Single molecule fluorescence spectroscopy. Single-molecule fluorescence experiments were conducted on a home-built confocal microscope equipped with a pulsed fiber laser (FemtoFiber pro TVIS, Toptica Photonics AG, Graefelfing, Germany) operating at 488 nm and a repetition rate of 80 MHz, with the pulses being synchronized with a diode-based laser (LDH P–C-485B, Picoquant GmbH, Berlin, Germany) operating at 485 nm and 20 MHz. A single-mode fiber (LMA-8, NKT Photonics, Birkerod, Denmark) was used for spatial filtering and a 60X microscope objective (UPlanApo 60x/1.20W, Olympus, Tokio, Japan) for excitation and fluorescence light collection. Dichroic beam splitters (Di01-R405/488/594-25x36, Semrock Inc./IDEX Corp., Lake Forest, IL, U.S.A., ZT594rdc, Chroma Technology Corp., Bellows Falls, VT, U.S.A) and a polarizing beam splitter (CVI Laser Optics, Albuquerque, NM, U.S.A.) were used to split the emission light and to guide it onto single-photon avalanche diodes (SPCM-AQRH-14-TR, Excelitas Technologies Corp., Mississauga, Canada) with their active areas serving as confocal pinholes. Spectral filters allowed to set the spectral range for the donor channel (LP496, BP25/50) and the acceptor channel (LP615, BP629/56), all filters were purchased from Semrock Inc (IDEX Corp., Lake Forest, IL, U.S.A.). Pulses from the detectors were fed into a TCSPC board (MultiHarp 150, Picoquant GmbH, Berlin, Germany) operating in the time-tagged time-resolved mode with 80 ps time resolution.

Single-molecule FRET (smFRET). Single-molecule FRET measurements were performed with 50–100 pM of Fmoc-synthetized doubly-labeled PTH_{84} in the presence of recombinantly produced PTH_{84} within the range of 10 μM to 500 μM. For burst experiments, a pulsed-interleaved excitation scheme was used with the donor molecule being excited with 80 MHz and 50 μW and the acceptor with 20 MHz and 10 μW. Detected photons were sorted by their arrival times with respect to a synchronization signal of 20 MHz for assignment to the respective excitation sources. Fluorescence bursts were identified using two threshold criteria, one threshold for the integrated emission after donor excitation and one for the acceptor emission after direct excitation of the acceptor to select for molecules bearing both a donor and acceptor, respectively. The first threshold was applied to a sliding density average of 10 adjacent photons detected by either of the two detection channels to avoid time binning. All consecutive photons above this threshold were combined into one burst and the minimum number of photons per burst was set to 100. Counted photons of each detector channel were corrected for background counts, quantum yields of fluorescence, and quantum efficiency of detection (including collection efficiency, filter transmission, spectral cross talk and detector efficiency). Averaging owing to conformational flexibility during transit through the focus was taken into consideration in the calculation of distances from energy transfer histograms using the integral

$$\langle E \rangle = \int P(r_{ee}) E(r_{ee}) dr_{ee}, \tag{2}$$

where $E(r_{ee}) = 1/(1 + (r_{ee}\ R_0^{-1})^6)$ is the distance dependence of the energy transfer with R_0 the characteristic Förster distance of 5.8 nm and $P(r_{ee})$ an excluded-volume probability distribution of the end-to-end distance approximated by the Gaussian-chain description:[74]

$$P(r_{ee}) = \left(\frac{3}{2\ \pi\ N\ b^2}\right)^{3/2} e^{-\frac{3\ r_{ee}}{2\ N\ b^2}} \tag{3}$$

where N is the sum of the number of amino acids between the dye labels and the apparent length of the dye linker in terms of b, and b the distance between two C_α-atoms, found as 0.38 nm.[75] The parameter r_{ee} can be used as a measure for the conformational space of a disordered chain (e.g. swollen, collapsed). For the high concentration, 4185 bursts were collected in total, while for the low concentration regime, individual energy transfer histograms of the samples with 40 μM, 50 μM, 60 μM and 70 μM were accumulated to obtain one plot (2835 bursts in total). A 2D analysis of the FRET efficiency and stoichiometry S was used to ensure that the displayed energy transfer values truly result from the energy transfer between donor and acceptor molecules, since molecules carrying a donor only would also apparently lead to low energy transfer values.[76] This photon distribution analysis is shown in Figure S4.

Fluorescence cross correlation spectroscopy (FCCS). The characteristic decay time of the translational diffusion was determined from the cross-correlation functions of the donor and the acceptor channel, $G(\tau)$, using the fitting function:

$$G(\tau) = \frac{1}{N}\left[1 - T + Texp\left(-\frac{\tau}{\tau_T}\right)\right]\left(1 + \left(\frac{\tau}{\tau_D}\right)^a\right)^{-1} * \left(1 + S^2\left(\frac{\tau}{\tau_D}\right)^a\right)^{-1/2} \tag{4}$$

where S and a are system parameters describing the shape of the focal volume, N is the average number of labeled molecules in the focal volume, and τ_D the average dwell time in the focus volume, being related to the inverse translational diffusion coefficient, D. Triplet blinking was parameterized by the triplet fraction, T, and triplet time, τ_T. The hydrodynamic radius, r_h was determined using the Stokes-Einstein equation with:

$$D = \frac{k_B T}{6\pi\eta r_h}, \tag{5}$$

where k_B is the Boltzmann constant, T the absolute temperature and η the viscosity of the solvent.[77] $G(\tau)$was normalized with

respect to the average number of molecules in the focus volume, $G_n(t) = G(\tau) \times N$. The reference measurements were conducted with Atto488 and Atto594.

Small angle X-ray scattering (SAXS). X-ray scattering experiments were performed in transmission mode using a SAXSLAB laboratory setup (Retro-F) equipped with an AXO micro-focus X-ray source. The AXO multilayer X-ray optic (AXO Dresden GmbH, Dresden, Germany) was used as a monochromator for Cu-K_α radiation ($\lambda =$ 0.154 nm). A two-dimensional detector (PILATUS3 R 300 K; DECTRIS, Baden, Switzerland) was used to record the 2D scattering patterns.

SAXS experiments were conducted using refillable capillaries with an outer diameter of 1 mm (BioSAS JSP stage, SAXSLAB/Xenocs, France). The intensities were angular-averaged and plotted versus the scattering angle q. The measurements were performed at room temperature and corrected for background, transmission and sample geometry. The measurement times were set to 6 h. Subsequent EOM analysis of the scattering intensities were conducted to reveal the most probable distributions of the radius of gyration, $p(r_g)$, and the end-to-end distances, $p(R_{ee})$ for 50 μM and 500 μM of PTH_{84}.[78–79]

Pulsed-Field-Gradient (PFG) NMR spectroscopy. The diffusion coefficient at different peptide concentrations was determined via PFG-NMR on the basis of proton spectra on a 600 MHz Bruker Avance III spectrometer. The gradient strength G was incremented in 26 steps from 2% to 98% of the maximum gradient $G_{max} =$ 0.53 T/m. The intensity for each gradient increment was integrated in the area 0.5 ppm–2.5 ppm. This resulting intensity decay was analyzed using the Stejskal-Tanner equation

$$\frac{I}{I_0} = e^{-D\,\gamma^2\,\sigma^2\,G^2\,\delta^2\,(\Delta - \frac{\delta}{3})} \tag{6}$$

where D is the diffusion coefficient, γ the gyromagnetic ratio of protons, σ the gradient shape factor ($2/\pi$ for the sine bell shape used in this work), G the gradient strength, δ the gradient length (6 ms) and Δ the diffusion time (100 ms).[80] The data were compared to the diffusion of the internal chemical shift reference substance DSS and converted to apparent hydrodynamic radii $r_{H,app}$ as

$$r_{H,app\ PTH} = \frac{D_{DSS}\ r_{H,DSS}}{D_{app,PTH}} \tag{7}$$

In an additional, similar experiment the r_H of DSS was calculated to be 0.339 nm, using 1,4-Dioxan ($r_H = 0.212$ nm) as a reference substance.[81] The obtained $r_{H,app}$ do not reflect a distinct state, but represents an average of the full ensemble of possible states within the sample. Hence, we only use it as a parameter indicating trends for the hydrodynamic properties.

Chemical shift perturbation (CSP) and signal intensity. ^{1}H-^{15}N-fHSQC spectra were acquired at different PTH_{84} concentrations on an 800 MHz Bruker Avance III spectrometer. The previously reported assignment of the cross-peaks was used.[58] The number of scans as a parameter to improve the signal-to-noise ratio was adjusted according to the sample concentration while the receiver gain was kept constant for all samples. Acquired spectra were processed using NMRPipe[82] and analyzed with PINT.[83–84] The change of the position of the cross peaks in ^{1}H-^{15}N-fHSQC spectra are expressed as the combined chemical shift $\Delta\delta$ and calculated as

$$\Delta\delta(^1H,\ ^{15}N) = \sqrt{(\delta\ ^1H)^2 + (\delta\ ^{15}N)^2} \tag{8}$$

with δ^1H and δ^{15}N the chemical shift difference between two spectra, given in Hz, in the direct and indirect dimension, respectively. For the analysis of the intensities of the cross peaks the signal intensity I was corrected for experimental details by

$$I = \frac{I_{exp}}{ns\ c_0} \tag{9}$$

where I_{exp} is the experimental intensity of a distinct cross-peak, ns the number of scans accumulated to acquire the ^{1}H-^{15}N-HSQC spectrum and c_0 the molar sample concentration. The samples contained 10% (v/v) D_2O and 0.01 mg/ml DSS as a reference substance for the chemical shift.

The absolute intensity of a cross-peak in an ^{1}H-^{15}N-fHSQC spectrum depends on many experimental and protein specific factors and therefore a direct quantification of protein populations is complex.[85] However, the change of relative intensities within a concentration series mostly results from differences in the transversal relaxation rate (R_2) due to changes of the local dynamics, the rotational correlation time or chemical exchange.[86–87] Therefore, the evolution of the cross-peak intensities as well as the CSP allows valuable insights to characterize the concentration dependence of PTH_{84} ^{1}H-^{15}N-fHSQC spectra. Due to slow tumbling of peptides incorporated into fibrils leading to broadening of cross-peaks beyond detection, only free, soluble peptides are expected to contribute to the acquired signal.

NMR relaxation experiments. The longitudinal (R_1) and transversal (R_2) relaxation rates were determined as pseudo-3D spectra on the basis of ^{1}H-^{15}N-fHSQC spectra as read-out on an 800 MHz Bruker Avance III spectrometer.[49] The respective rates were extracted from the mono-exponential decay over 8 points (0 ms–1000 ms for R_1; 0 ms–192 ms for R_2) of recovery time. Relaxation experiments were conducted for samples containing 20 μM, 100 μM, 250 μM and 500 μM ^{15}N-labelled PTH_{84}. Due to the reduced sensitivity of NMR relaxation experiments compared to ^{1}H-^{15}N-fHSQC, it was not possible to acquire reliable relaxation data for regime I to compare with the purely monomeric state. To analyze the relaxation properties of soluble PTH_{84} in equilibrium with fibrils, a 100 μM ^{15}N labelled sample was incubated with 5% pre-formed unlabeled seeds for 20 h prior to the measurement.

CSP-RMSD analysis. ^{1}H-^{15}N-fHSQC spectra of samples containing 100 μM, 250 μM or 500 μM ^{15}N-PTH_{84} were acquired before and 7 days after addition of 5% unlabeled pre-formed seeds (given in monomer equivalents). The incubation time of 7 days was chosen to ensure that the system reached the thermodynamic equilibrium. Directly prior to the measurement, the samples were carefully mixed to resuspend settled fibrils. The chemical shift differences $\Delta\delta$ between these sample spectra and a set of fibril-free reference spectra in a range of 5 μM $< c_0 <$ 500 μM were used to compare the soluble state in the presence of fibrils with the prenucleation equilibrium. As a measure for the overall CSP between a sample and each reference spectrum we then calculated the root mean square deviation (RMSD) for each pair of spectra as

$$\mathrm{RMSD} = \sqrt{\frac{(\Delta\delta_1)^2 + (\Delta\delta_2)^2 + \ldots + (\Delta\delta_n)^2}{n}} \tag{10}$$

This experiment allows to study the soluble peptide fraction also in the presence of fibrils, as the signal width of ^{15}N labelled PTH_{84} eventually incorporated into fibrils would broaden beyond detection due to slow tumbling. In order to obtain information about the time dependence, we added 10% unlabeled pre-formed seeds at time zero (directly before spectra acquisition) and repeated the

acquisition of ^{1}H spectra to monitor the concentration of NMR detectable, soluble PTH_{84} and ^{1}H-^{15}N-fHSQC spectra to follow the time dependence of the CSP for two samples with $c_0 = 250\ \mu M$ and 500 μM. For each time point, the RMSD values of the CSP between the sample spectra and the fibril-free reference spectra have been conducted as stated above. The integrals from 2.4 ppm to 0 ppm from the ^{1}H spectra were used to estimate the overall concentration of soluble peptide.

Acknowledgements

We acknowledge funding from the Federal Ministry for Education and Research (BMBF, 03Z22HN22), the European Regional Development Funds (EFRE, ZS/2016/04/78115 and for the support of the NMR infrastructure), the MLU Halle-Wittenberg, the JGU Mainz and the German research foundation (DFG, project ID 189853844 – TRR 102 "polymers under multiple constraints", TP A12 and TP B12, and project ID 391498659 – RTG 2467 "Intrinsically Disordered Proteins – Molecular Principles, Cellular Functions, and Diseases", TP 1, TP 2 and TP 11). The authors thank Jakob Schneider for initial studies on the project, Sven Rothemund for the synthesis of Atto488/Atto594 labelled PTH_{84} as well as Malte Neudorf, Ulrich Weininger and Stefan Gröger for valuable discussions. Open Access funding enabled and organized by Projekt DEAL.

Conflict of Interests

The authors declare no conflict of interest.

Data Availability Statement

The data that support the findings of this study are available from the corresponding author upon reasonable request.

Keywords: biophysics · functional amyloids · peptide hormone · nucleation · critical concentration

[1] F. Chiti, C. M. Dobson, *Annu. Rev. Biochem.* **2006**, *75*, 333–366.
[2] J. T. Jarrett, P. T. Lansbury Jr., *Cell* **1993**, *73*, 1055–1058.
[3] P. T. Lansbury, H. A. Lashuel, *Nature* **2006**, *443*, 774–779.
[4] J. D. Sipe, M. D. Benson, J. N. Buxbaum, S. Ikeda, G. Merlini, M. J. Saraiva, P. Westermark, *Amyloid* **2012**, *19*, 167–170.
[5] Y. Shikama, J. Kitazawa, N. Yagihashi, O. Uehara, Y. Murata, N. Yajima, R. Wada, S. Yagihashi, *Intern. Med.* **2010**, *49*, 397–401.
[6] J. N. Buxbaum, J. V. Chuba, G. C. Hellman, A. Solomon, G. R. Gallo, *Ann. Intern. Med.* **1990**, *112*, 455–464.
[7] D. M. Fowler, A. V. Koulov, C. Alory-Jost, M. S. Marks, W. E. Balch, J. W. Kelly, *PLoS Biol.* **2006**, *4*, e6.
[8] M. R. Chapman, L. S. Robinson, J. S. Pinkner, R. Roth, J. Heuser, M. Hammar, S. Normark, S. J. Hultgren, *Science* **2002**, *295*, 851–855.
[9] R. Hervas, M. J. Rau, Y. Park, W. Zhang, A. G. Murzin, J. A. J. Fitzpatrick, S. H. W. Scheres, K. Si, *Science* **2020**, *367*, 1230–1234.
[10] S. K. Maji, M. H. Perrin, M. R. Sawaya, S. Jessberger, K. Vadodaria, R. A. Rissman, P. S. Singru, K. P. Nilsson, R. Simon, D. Schubert, D. Eisenberg, J. Rivier, P. Sawchenko, W. Vale, R. Riek, *Science* **2009**, *325*, 328–332.
[11] K. C. Evans, E. P. Berger, C. G. Cho, K. H. Weisgraber, P. T. Lansbury Jr., *Proc. Natl. Acad. Sci. USA* **1995**, *92*, 763–767.
[12] L. Nielsen, R. Khurana, A. Coats, S. Frokjaer, J. Brange, S. Vyas, V. N. Uversky, A. L. Fink, *Biochemistry* **2001**, *40*, 6036–6046.
[13] S. I. Cohen, M. Vendruscolo, M. E. Welland, C. M. Dobson, E. M. Terentjev, T. P. Knowles, *J. Chem. Phys.* **2011**, *135*, 065105.
[14] T. C. T. Michaels, A. Šarić, J. Habchi, S. Chia, G. Meisl, M. Vendruscolo, C. M. Dobson, T. P. J. Knowles, *Annu. Rev. Phys. Chem.* **2018**, *69*, 273–298.
[15] M. Törnquist, T. C. T. Michaels, K. Sanagavarapu, X. Yang, G. Meisl, S. I. A. Cohen, T. P. J. Knowles, S. Linse, *Chem. Commun.* **2018**, *54*, 8667–8684.
[16] M. Törnquist, S. Linse, *Angew. Chem. Int. Ed.* **2021**, *60*, 24008–24011.
[17] J. D. Harper, P. T. Lansbury Jr., *Annu. Rev. Biochem.* **1997**, *66*, 385–407.
[18] B. O'Nuallain, S. Shivaprasad, I. Kheterpal, R. Wetzel, *Biochemistry* **2005**, *44*, 12709–12718.
[19] R. Wetzel, *Acc. Chem. Res.* **2006**, *39*, 671–679.
[20] R. Crespo, F. A. Rocha, A. M. Damas, P. M. Martins, *J. Biol. Chem.* **2012**, *287*, 30585–30594.
[21] M. Gopalswamy, A. Kumar, J. Adler, M. Baumann, M. Henze, S. T. Kumar, M. Fändrich, H. A. Scheidt, D. Huster, J. Balbach, *Biochim. Biophys. Acta* **2015**, *1854*, 249–257.
[22] L. M. Lauth, B. Voigt, T. Bhatia, L. Machner, J. Balbach, M. Ott, *FEBS Lett.* **2022**, *596*, 2928–2939.
[23] B. Voigt, M. Ott, J. Balbach, *Macromol. Biosci.* **2023**, e2200525.
[24] A. J. Baldwin, T. P. Knowles, G. G. Tartaglia, A. W. Fitzpatrick, G. L. Devlin, S. L. Shammas, C. A. Waudby, M. F. Mossuto, S. Meehan, S. L. Gras, J. Christodoulou, S. J. Anthony-Cahill, P. D. Barker, M. Vendruscolo, C. M. Dobson, *J. Am. Chem. Soc.* **2011**, *133*, 14160–14163.
[25] M. So, D. Hall, Y. Goto, *Curr. Opin. Struct. Biol.* **2016**, *36*, 32–39.
[26] A. J. Dear, G. Meisl, A. Šarić, T. C. T. Michaels, M. Kjaergaard, S. Linse, T. P. J. Knowles, *Chem. Sci.* **2020**, *11*, 6236–6247.
[27] G. A. Garcia, S. I. Cohen, C. M. Dobson, T. P. Knowles, *Phys. Rev. E* **2014**, *89*, 032712.
[28] A. Ceccon, V. Tugarinov, R. Ghirlando, G. M. Clore, *Proc. Natl. Acad. Sci. USA* **2020**, *117*, 5844–5852.
[29] S. A. Kotler, V. Tugarinov, T. Schmidt, A. Ceccon, D. S. Libich, R. Ghirlando, C. D. Schwieters, G. M. Clore, *Proc. Natl. Acad. Sci. USA* **2019**, *116*, 3562–3571.
[30] T. K. Karamanos, M. P. Jackson, A. N. Calabrese, S. C. Goodchild, E. E. Cawood, G. S. Thompson, A. P. Kalverda, E. W. Hewitt, S. E. Radford, *eLife* **2019**, *8*, e46574.
[31] Z. Hall, C. Schmidt, A. Politis, *J. Biol. Chem.* **2016**, *291*, 4626–4637.
[32] E. Rennella, T. Cutuil, P. Schanda, I. Ayala, F. Gabel, V. Forge, A. Corazza, G. Esposito, B. Brutscher, *J. Mol. Biol.* **2013**, *425*, 2722–2736.
[33] F. Hasecke, T. Miti, C. Perez, J. Barton, D. Schölzel, L. Gremer, C. S. R. Grüning, G. Matthews, G. Meisl, T. P. J. Knowles, D. Willbold, P. Neudecker, H. Heise, G. Ullah, W. Hoyer, M. Muschol, *Chem. Sci.* **2018**, *9*, 5937–5948.
[34] C. Perez, T. Miti, F. Hasecke, G. Meisl, W. Hoyer, M. Muschol, G. Ullah, *J. Phys. Chem. B* **2019**, *123*, 5678–5689.
[35] P. H. Nguyen, A. Ramamoorthy, B. R. Sahoo, J. Zheng, P. Faller, J. E. Straub, L. Dominguez, J. E. Shea, N. V. Dokholyan, A. De Simone, B. Ma, R. Nussinov, S. Najafi, S. T. Ngo, A. Loquet, M. Chiricotto, P. Ganguly, J. McCarty, M. S. Li, C. Hall, Y. Wang, Y. Miller, S. Melchionna, B. Habenstein, S. Timr, J. Chen, B. Hnath, B. Strodel, R. Kayed, S. Lesné, G. Wei, F. Sterpone, A. J. Doig, P. Derreumaux, *Chem. Rev.* **2021**, *121*, 2545–2647.
[36] U. I. Gerling, M. S. Miettinen, B. Koksch, *ChemPhysChem* **2015**, *16*, 108–114.
[37] J. F. Habener, M. Rosenblatt, J. T. Potts Jr., *Physiol. Rev.* **1984**, *64*, 985–1053.
[38] T. J. Anderson, S. W. Ewen, *J. Clin. Pathol.* **1974**, *27*, 656–663.
[39] J. Jumper, R. Evans, A. Pritzel, T. Green, M. Figurnov, O. Ronneberger, K. Tunyasuvunakool, R. Bates, A. Žídek, A. Potapenko, A. Bridgland, C. Meyer, S. A. A. Kohl, A. J. Ballard, A. Cowie, B. Romera-Paredes, S. Nikolov, R. Jain, J. Adler, T. Back, S. Petersen, D. Reiman, E. Clancy, M. Zielinski, M. Steinegger, M. Pacholska, T. Berghammer, S. Bodenstein, D. Silver, O. Vinyals, A. W. Senior, K. Kavukcuoglu, P. Kohli, D. Hassabis, *Nature* **2021**, *596*, 583–589.
[40] U. C. Marx, K. Adermann, P. Bayer, W. G. Forssmann, P. Rösch, *Biochem. Biophys. Res. Commun.* **2000**, *267*, 213–220.
[41] M. Varadi, S. Anyango, M. Deshpande, S. Nair, C. Natassia, G. Yordanova, D. Yuan, O. Stroe, G. Wood, A. Laydon, A. Žídek, T. Green, K. Tunyasuvunakool, S. Petersen, J. Jumper, E. Clancy, R. Green, A. Vora, M. Lutfi, M. Figurnov, A. Cowie, N. Hobbs, P. Kohli, G. Kleywegt, E. Birney, D. Hassabis, S. Velankar, *Nucleic Acids Res.* **2022**, *50*, D439-D444.

[42] S. Sachan, C. G. Moya, B. Voigt, M. Köhn, J. Balbach, *FEBS Lett.* **2023**, *597*, 995–1006.
[43] K. Hasegawa, K. Ono, M. Yamada, H. Naiki, *Biochemistry* **2002**, *41*, 13489–13498.
[44] C. L. Pashley, E. W. Hewitt, S. E. Radford, *J. Mol. Biol.* **2016**, *428*, 631–643.
[45] T. R. Alderson, I. Pritišanac, A. M. Moses, J. D. Forman-Kay, **2022**, bioRxiv preprint DOI: 10.1101/2022.02.18.481080.
[46] A. Micsonai, F. Wien, L. Kernya, Y. H. Lee, Y. Goto, M. Réfrégiers, J. Kardos, *Proc. Natl. Acad. Sci. USA* **2015**, *112*, E3095-E3103.
[47] E. Gasteiger, C. Hoogland, A. Gattiker, S. Duvaud, M. R. Wilkins, R. D. Appel, A. Bairoch, in *The Proteomics Protocols Handbook* (Ed.: J. M. Walker), Humana Press, Totowa, NJ, **2005**, pp. 571–607.
[48] H. J. Dyson, P. E. Wright, *Nat. Struct. Biol.* **1998**, *5 Suppl*, 499–503.
[49] T. Gruber, M. Lewitzky, L. Machner, U. Weininger, S. M. Feller, J. Balbach, *J. Mol. Biol.* **2022**, *434*, 167407.
[50] N. Tjandra, S. E. Feller, R. W. Pastor, A. Bax, *J. Am. Chem. Soc.* **1995**, *117*, 12562–12566.
[51] A. G. Palmer, 3rd, *Curr. Opin. Struct. Biol.* **1997**, *7*, 732–737.
[52] J. Wen, L. Hong, G. Krainer, Q. Q. Yao, T. P. J. Knowles, S. Wu, S. Perrett, *J. Am. Chem. Soc.* **2021**, *143*, 13056–13064.
[53] D. Ubbiali, M. Fratini, L. Piersimoni, C. H. Ihling, M. Kipping, I. Heilmann, C. Iacobucci, A. Sinz, *Angew. Chem. Int. Ed.* **2022**, *61*, e202205726.
[54] A. Ceccon, V. Tugarinov, G. M. Clore, *J. Phys. Chem. Lett.* **2020**, *11*, 5643–5648.
[55] A. Ceccon, V. Tugarinov, F. Torricella, G. M. Clore, *Proc. Natl. Acad. Sci. USA* **2022**, *119*, e2207690119.
[56] G. Platzer, M. Okon, L. P. McIntosh, *J. Biomol. NMR* **2014**, *60*, 109–129.
[57] H. N. Raum, U. Weininger, *ChemBioChem* **2019**, *20*, 922–930.
[58] Z. Evgrafova, B. Voigt, M. Baumann, M. Stephani, W. H. Binder, J. Balbach, *ChemPhysChem* **2019**, *20*, 236–240.
[59] J. Heyda, P. E. Mason, P. Jungwirth, *J. Phys. Chem. B* **2010**, *114*, 8744–8749.
[60] K. Kumar, S. M. Woo, T. Siu, W. A. Cortopassi, F. Duarte, R. S. Paton, *Chem. Sci.* **2018**, *9*, 2655–2665.
[61] S. M. Liao, Q. S. Du, J. Z. Meng, Z. W. Pang, R. B. Huang, *Chem. Cent. J.* **2013**, *7*, 44.
[62] R. M. Vernon, P. A. Chong, B. Tsang, T. H. Kim, A. Bah, P. Farber, H. Lin, J. D. Forman-Kay, *eLife* **2018**, *7*, e31486.
[63] N. L. Fawzi, D. S. Libich, J. Ying, V. Tugarinov, G. M. Clore, *Angew. Chem. Int. Ed.* **2014**, *53*, 10345–10349.
[64] N. L. Fawzi, J. Ying, R. Ghirlando, D. A. Torchia, G. M. Clore, *Nature* **2011**, *480*, 268–272.
[65] S. De Sio, J. Waegele, T. Bhatia, B. Voigt, H. Lilie, M. Ott, *Macromol. Biosci.* **2023**, e2200527.
[66] Y. R. Huang, R. T. Liu, *Int. J. Mol. Sci.* **2020**, *21*, 447.
[67] C. Piotrowski, C. H. Ihling, A. Sinz, *Methods* **2015**, *89*, 121–127.
[68] J. Wägele, S. De Sio, B. Voigt, J. Balbach, M. Ott, *Biophys. J.* **2019**, *116*, 227–238.
[69] E. D. Drew, R. W. Janes, *Nucleic Acids Res.* **2020**, *48*, W17-W24.
[70] F. Sobott, H. Hernández, M. G. McCammon, M. A. Tito, C. V. Robinson, *Anal. Chem.* **2002**, *74*, 1402–1407.
[71] J. L. Benesch, B. T. Ruotolo, D. A. Simmons, C. V. Robinson, *Chem. Rev.* **2007**, *107*, 3544–3567.
[72] H. Hernández, C. V. Robinson, *Nat. Protoc.* **2007**, *2*, 715–726.
[73] N. Morgner, C. V. Robinson, *Anal. Chem.* **2012**, *84*, 2939–2948.
[74] M. Doi, S. F. Edwards, *The theory of polymer dynamics*, The Clarendon Press, Oxford University Press, New York, **1986**.
[75] H. Hofmann, A. Soranno, A. Borgia, K. Gast, D. Nettels, B. Schuler, *Proc. Natl. Acad. Sci. USA* **2012**, *109*, 16155–16160.
[76] B. Hellenkamp, S. Schmid, O. Doroshenko, O. Opanasyuk, R. Kühnemuth, S. Rezaei Adariani, B. Ambrose, M. Aznauryan, A. Barth, V. Birkedal, M. E. Bowen, H. Chen, T. Cordes, T. Eilert, C. Fijen, C. Gebhardt, M. Götz, G. Gouridis, E. Gratton, T. Ha, P. Hao, C. A. Hanke, A. Hartmann, J. Hendrix, L. L. Hildebrandt, V. Hirschfeld, J. Hohlbein, B. Hua, C. G. Hübner, E. Kallis, A. N. Kapanidis, J. Y. Kim, G. Krainer, D. C. Lamb, N. K. Lee, E. A. Lemke, B. Levesque, M. Levitus, J. J. McCann, N. Naredi-Rainer, D. Nettels, T. Ngo, R. Qiu, N. C. Robb, C. Röcker, H. Sanabria, M. Schlierf, T. Schröder, B. Schuler, H. Seidel, L. Streit, J. Thurn, P. Tinnefeld, S. Tyagi, N. Vandenberk, A. M. Vera, K. R. Weninger, B. Wünsch, I. S. Yanez-Orozco, J. Michaelis, C. A. M. Seidel, T. D. Craggs, T. Hugel, *Nat. Methods* **2018**, *15*, 669–676.
[77] C. C. Miller, J. Walker, *Proc. Math. Phys. Eng. Sci.* **1924**, *106*, 724–749.
[78] A. Sagar, C. M. Jeffries, M. V. Petoukhov, D. I. Svergun, P. Bernadó, *J. Chem. Theory Comput.* **2021**, *17*, 2014–2021.
[79] G. Tria, H. D. Mertens, M. Kachala, D. I. Svergun, *IUCrJ* **2015**, *2*, 207–217.
[80] E. O. Stejskal, J. E. Tanner, *J. Chem. Phys.* **1965**, *42*, 288–292.
[81] D. K. Wilkins, S. B. Grimshaw, V. Receveur, C. M. Dobson, J. A. Jones, L. J. Smith, *Biochemistry* **1999**, *38*, 16424–16431.
[82] F. Delaglio, S. Grzesiek, G. W. Vuister, G. Zhu, J. Pfeifer, A. Bax, *J. Biomol. NMR* **1995**, *6*, 277–293.
[83] A. Ahlner, M. Carlsson, B.-H. Jonsson, P. Lundström, *J. Biomol. NMR* **2013**, *56*, 191–202.
[84] M. Niklasson, R. Otten, A. Ahlner, C. Andresen, J. Schlagnitweit, K. Petzold, P. Lundström, *J. Biomol. NMR* **2017**, *69*, 93–99.
[85] M. Dreydoppel, J. Balbach, U. Weininger, *J. Biomol. NMR* **2022**, *76*, 3–15.
[86] W. Becker, K. C. Bhattiprolu, N. Gubensäk, K. Zangger, *ChemPhysChem* **2018**, *19*, 895–906.
[87] J. Jeener, B. H. Meier, P. Bachmann, R. R. Ernst, *J. Chem. Phys.* **1979**, *71*, 4546–4553.

Manuscript received: June 22, 2023
Revised manuscript received: July 18, 2023
Accepted manuscript online: July 21, 2023
Version of record online: August 3, 2023